Fluid Dynamics &
Materials Processing

Tech Science Press

http://doi.org/10.32604/fdmp.2026.076554

ARTICLE

Variable-Diameter Finned-Tube Heat Exchanger Optimization for R290 Split Air Conditioners

Zheming Cheng[1,*], Xinping Ouyang[2], Leren Tao[2], Ke Sun[2] and Zihao Wang[2]

[1]School of Mechanical and Electrical Engineering, Zhoukou Normal University, Wenchang Rd, Zhoukou, China
[2]School of Energy and Power Engineering, University of Shanghai for Science and Technology, 516 Jungong Rd, Shanghai, China
*Corresponding Author: Zheming Cheng. Email: czm0224@163.com

Received: 22 November 2025; Accepted: 09 May 2026; Published: 27 May 2026

ABSTRACT: Balancing heat transfer performance with material cost and refrigerant charge remains a key challenge in split air conditioning systems. To address this issue, the present study proposes a finned-tube heat exchanger with a variable-diameter configuration, combining 5.2 mm and 7.3 mm tubes for use with R290 refrigerant. Three hybrid arrangements are examined against a conventional baseline with uniform 7.3 mm tubes, differing in the number and spacing of the 5.2 mm tubes integrated within the heat exchanger layout, thereby enabling targeted structural and thermal optimization of the indoor unit. An integrated methodology, based on a theoretical iterative algorithm and supported by numerical simulations and experimental validation, is employed to characterize heat transfer and fluid flow under rated cooling conditions. The results show that the proposed configurations achieve substantial reductions in refrigerant charge, by up to 11.5%, and copper usage, by up to 7.78%, while simultaneously enhancing the system coefficient of performance by as much as 3.75% compared to the reference design. Configurations with a higher proportion and tighter spacing of 5.2 mm tubes yield the greatest improvement in energy efficiency, whereas those maximizing the substitution of 7.3 mm tubes with 5.2 mm tubes achieve the most pronounced reductions in material usage and refrigerant charge. Overall, the findings demonstrate that variable-diameter tube heat exchangers provide an effective strategy for optimizing the trade-off between performance, cost, and environmental impact in R290-based split air conditioning systems.

KEYWORDS: Variable tube diameter; split air conditioner (SAC); indoor unit; R290; numerical simulation; structural optimization

1 Introduction

Energy efficiency and environmental protection are global priorities, leading governments and international organizations to implement stringent regulations for electrical equipment. Household appliances, which account for a substantial portion of global energy consumption, are a key focus of these efforts. Among them, Split Air Conditioners (SAC) are widely used to provide thermal comfort, sustaining a high global demand. Consequently, SAC development is increasingly focused on enhancing efficiency, environmental performance, and comfort, with significant research attention directed toward optimizing the indoor unit [1]. As illustrated in Fig. 1, a typical SAC indoor unit comprises several key components, including an air inlet grille, a finned-tube heat exchanger, a cross-flow fan, an air outlet, and the unit housing, all of which have been the subject of extensive research to improve overall system performance.

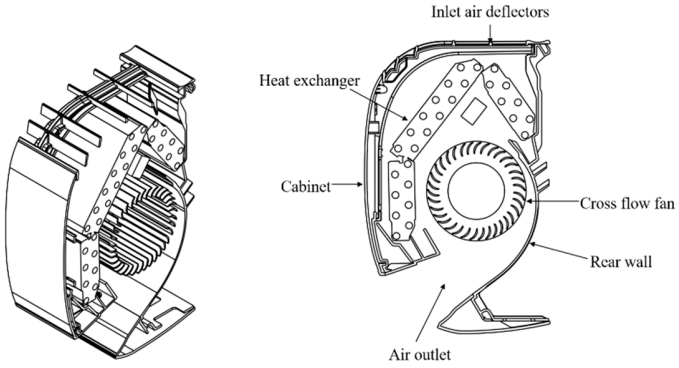

Figure 1: SAC indoor unit structure diagram.

Significant research efforts have been dedicated to optimizing individual components of SAC indoor units, primarily focusing on the cross-flow fan, the finned-tube heat exchanger, and the refrigerant itself.

Regarding the cross-flow fan (CFF), studies have focused on its geometric parameters and internal flow dynamics. For instance, Özer et al. [2] conducted a parametric study on the CFF cabinet, examining the individual and interactive effects of volute curvature, tongue angle, and vortex wall distance on flow behavior. Concurrently, Zou et al. [3] integrated PIV measurements with 3D unsteady numerical simulations, revealing a non-uniform axial flow distribution with pronounced three-dimensional characteristics. They demonstrated that structural optimization based on this 3D flow analysis could significantly improve both aerodynamic and aero acoustic performance. These studies collectively underscore the importance of precise fan and casing design for overall unit efficiency and noise reduction.

In parallel, substantial research efforts have been dedicated to enhancing air-side heat transfer and flow performance through the exploration of diverse fin geometries and configurations. Feleke et al. [4] numerically investigated the effects of louver edge configurations (vertical, inclined, and horizontal) on the thermo-hydraulic performance of louvered-fin compact heat exchangers under varying louver angles and inlet air velocities ranging from 1 to 30 m/s. Their results revealed that the horizontal edge configuration reduced pressure drop by up to 24.2%, accompanied by only a 1.01% increase in outlet air temperature compared with the inclined edge. This finding indicates that louver edge design exerts a significant impact on pressure drop characteristics while imposing a relatively minor influence on thermal performance. Torbarina et al. [5] analyzed slotted finned-tube heat exchangers and concluded that increasing fin spacing reduces pressure drop, yet the heat transfer flux density exhibits diminishing returns beyond a critical threshold. They also identified a performance trade-off associated with thicker fins, which enhance heat transfer but simultaneously escalate air-side pressure drop. Batista et al. [6] evaluated the influence of rectangular fin geometric parameters on the thermal performance of cross-flow air-water finned-tube heat exchangers. Their results demonstrated that elevated fin height induces a higher air-side pressure drop; moreover, convective heat transfer intensity initially increases with fin height but declines after exceeding a specific value. The heat exchanger achieved the maximum JF coefficient when fin height equaled half the fin span. Further investigations on wavy fins [7] and trapezoidal slit fins [8] consistently validate that geometric optimization constitutes a pivotal strategy for improving air-side thermal-hydraulic performance. Complementing these geometric-oriented studies, Wei et al. [9] experimentally examined the condensation retention capacity and air-side performance of finned-tube heat exchangers under varied fin spacing and surface treatment conditions. Their results demonstrated that hydrophilic surface treatment effectively enhances heat transfer efficiency and condensation drainage capability while mitigating air-side pressure loss. Additionally, Azzouz et al. [10] explored the effect of ultrasonic excitation on the heat transfer rate of

finned-plate tube heat exchangers, revealing that the efficacy of ultrasonic excitation can be strengthened by reducing the flow rate, ambient temperature, and air passage velocity.

On the refrigerant side, enhanced heat transfer, particularly in-tube boiling, is crucial. A significant body of literature has focused on micro-ribbed tubes. Cho et al. [11] and Alnaimat et al. [12] both found that micro-ribbed tubes substantially improve the boiling heat transfer coefficient compared to smooth tubes, with performance dependent on factors like mass flow rate, fin height, and the refrigerant used. Celen et al. [13] quantified this improvement, reporting that micro-ribbed tubes exhibited 1.4 to 1.9 times higher boiling heat transfer coefficients, albeit with a 1.5 to 3.0 times higher pressure drop. Concurrently, studies on small-diameter tubes by Oh et al. [14] revealed that reducing tube diameter increases the average heat transfer coefficient due to intensified boiling nucleation.

Despite these advancements, a critical review of the existing literature reveals a clear gap. Research on heat exchanger tubes has largely pursued two distinct paths: enhancing heat transfer through complex internal geometries (e.g., micro-ribs) or exploiting the benefits of uniformly small diameters. While effective in boosting heat transfer, these approaches each introduce significant drawbacks. The use of small-diameter tubes, for example, leads to a substantial increase in refrigerant-side pressure drop, which can degrade overall system efficiency. To address this, a novel concept of variable-diameter heat exchangers has been proposed, which strategically combines small and large diameter tubes. Wu et al. [15] demonstrated that a finned-tube heat exchanger with a 6 mm tube in the first row and a 13.2 mm tube in the second row improved heat transfer while reducing pressure drop compared to a traditional uniform-diameter design. This variable-diameter approach offers a promising pathway to balance heat transfer enhancement against the penalty of increased pressure drop [16].

Furthermore, the global push for environmental protection has redirected attention to refrigerants with lower global warming potential. R290 has emerged as a natural, eco-friendly alternative with excellent thermophysical properties, leading to higher system energy efficiency [17]. However, its adoption is hindered by its A3 flammability rating [18], making it imperative to minimize its charge in the system. The variable-diameter heat exchanger, by reducing the internal volume, presents an ideal solution for safely utilizing R290 in split air conditioners.

While the concept of variable-diameter heat exchangers shows promise, and R290 is a compelling refrigerant, prior research offers limited guidance on their optimal integration. Specifically, there is a lack of systematic investigation into the combined effect of tube diameter configuration and R290's unique flow and heat transfer characteristics. No existing study has comprehensively optimized the variable-diameter heat exchanger design specifically for R290, nor has it fully characterized the complex interplay between the refrigerant-side behavior (in tubes of varying diameters) and the air-side performance within the same unit.

To address these critical gaps, this study adopts an integrated methodology combining theoretical calculations with numerical simulations. The simulation model is rigorously validated against experimental data to ensure its reliability. The primary objectives of this work are: (1) to characterize the heat transfer and pressure drop behavior of R290 in variable-diameter heat exchangers; (2) to identify the most effective tube diameter configuration for maximizing overall system performance; and (3) to systematically analyze how different tube configurations influence both air-side heat transfer and airflow behavior, as well as refrigerant-side heat transfer and pressure drop. The findings of this study aim to provide a novel and practical design strategy for developing high-efficiency, low-charge R290 split air conditioners.

2 Theoretical Calculation

Research progresses on heat exchangers with variable tube diameters remain insufficient thus far. On the basis of conventional evaporator design theories, this study establishes a relevant theoretical calculation framework. To evaluate the heat transfer and flow resistance characteristics of the indoor unit, a four-module iterative algorithm is adopted, as illustrated in Figs. 2 and 3. The iterative procedure comprehensively takes into account the tube wall temperature, overall heat transfer capacity, in-tube pressure loss, and pressure fluctuation induced by sudden diameter expansion of variable-diameter tubes in the indoor unit.

In this computational framework, the front and rear calculation stages are exemplified by small-diameter and large-diameter tubes, respectively. The proposed approach also offers an effective solution to acquire tube wall temperature parameters, which can provide essential boundary conditions for subsequent three-dimensional numerical simulation of the outer tube side.

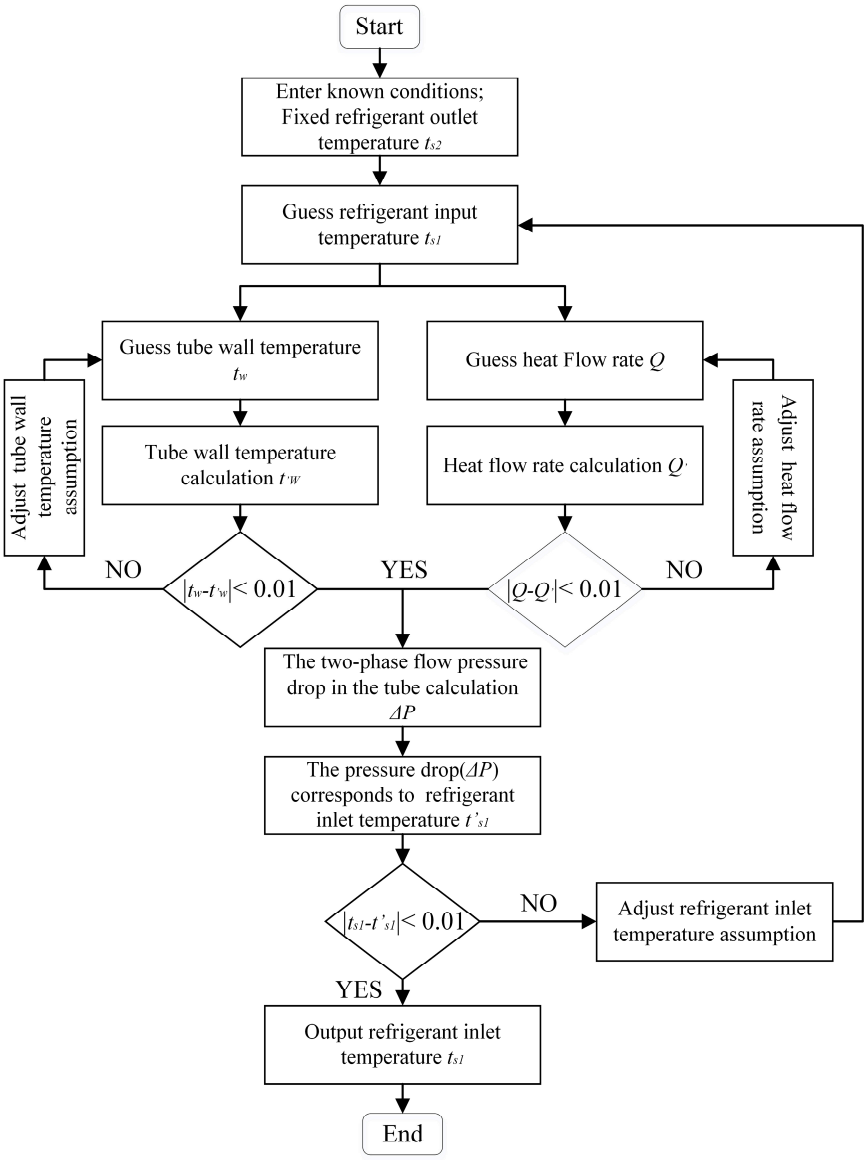

Figure 2: Iterative method for the association of wall temperature, heat exchange and pressure drop inside the tube.

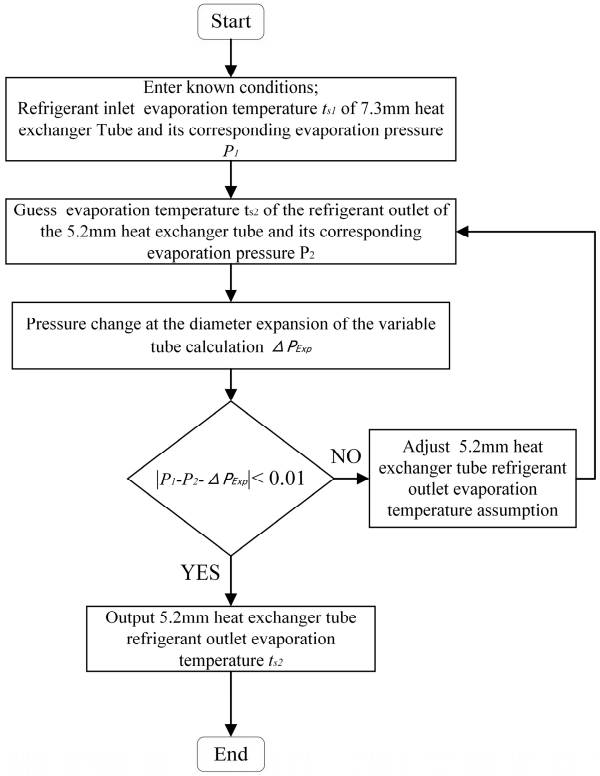

Figure 3: Iterative method for pressure drop change at the sudden expansion of variable tube diameter.

2.1 Calculation of Indoor Unit Heat Exchanger Capacity and Tube Wall Temperature

2.1.1 Air-Side Heat Transfer Coefficient

The j-factor for the heat transfer coefficient of the air outside the tube is calculated using Eq. (1) [19]

$$j = 1.0691\mathrm{Re}\frac{j_4}{f}\left(\frac{s_f-\delta_f}{d_b}\right)^{j_5}\left(\frac{s_s}{s_h}\right)N^{j_7} \tag{1}$$

where,

$$j_4 = -0.535 + 0.017\left(\frac{s_1}{s_2}\right) - 0.0107N \tag{2}$$

$$j_5 = 0.4155 + 5.5756\sqrt{\frac{N}{\mathrm{Re}_f}}\ln\frac{N}{\mathrm{Re}_f} + 24.2028\sqrt{\frac{N}{\mathrm{Re}_f}} \tag{3}$$

$$j_6 = 0.2646 + 1.0491\left(\frac{s_s}{s_h}\right)\ln\frac{s_s}{s_h} - 0.216\left(\frac{s_s}{s_h}\right)^3 \tag{4}$$

$$j_7 = 0.3749 + 0.0046\sqrt{\mathrm{Re}_f}\ln\mathrm{Re}_f - 0.0433\sqrt{\mathrm{Re}_f} \tag{5}$$

where, s_f is the fin pitch, δ_f is the fin thickness, d_b is the fin root diameter, s_s is the open slit width, s_h is the open slit height and N is the number of rows of heat exchanger tube, s_1 is the horizontal tube spacing, mm; s_2 is the vertical tube spacing, mm.

The wind speed at the narrowest ventilation surface [19] is:

$$w_{\max} = \frac{q_{va}}{HB\sigma} \tag{6}$$

where, H is the evaporator height, m; B is the effective length of the single tube, m; σ is the narrowest circulation area and the ratio of the wind area.

The heat transfer coefficient outside the tube [19] is:

$$\alpha_0 = \frac{j\rho_{am} w_{\max} c_{pa}}{\mathrm{Pr}^{\frac{2}{3}}} \tag{7}$$

where, ρ_{am} is the density of air at the average temperature, kg/m^3; c_{pa} is the specific heat capacity of air at the average temperature, J/(kg·K); Pr_a is the prandtl number of the air at the average temperature.

Moisture Separation Coefficient [19]:

$$\xi = 1 + 2.46\frac{d_m - d_w}{t_m - t_w} \tag{8}$$

Rib efficiency [19]:

$$\eta_f = \frac{\tanh(mh')}{mh'} \tag{9}$$

Equivalent surface heat transfer coefficient on the air side [19]

$$\alpha_j = \xi\alpha_0\left(\frac{\eta_f f_f + f_b}{f_t}\right) \tag{10}$$

where, f_t for the total surface area outside the tube, m^2; f_f for the area of fins outside the tube, m^2; f_b for the outer surface area of the tube between the fins, m^2.

The aforementioned calculation assumes that the air enters the tube bundle perpendicular to the tube axis direction and that the flow rate is evenly distributed throughout the bundle.

2.1.2 Refrigerant Side Heat Transfer Coefficient

Calculation criterion for boiling heat exchange of refrigerant in micro finned tubes Eq. (11) [20]:

$$\alpha_i = \alpha_L\left[c_1 Bo^{c_2}\left(\frac{p_0 d_i}{\sigma}\right)^{c_3} + c_4\left(\frac{1}{X_{tt}}\right)^{c_5}\left(\frac{gf}{\mu_L}\right)^{c_6}\right] \times \mathrm{Re}_L{}^{c_7}\mathrm{Pr}_L{}^{c_8}\left(\frac{\delta}{f}\right)^{c_9} \tag{11}$$

where, $c_1 = 0.009622$, $c_2 = 0.1106$, $c_3 = 0.3814$, $c_4 = 7.685$, $c_5 = 0.51$, $c_6 = -0.736$, $c_7 = 0.2045$, $c_8 = 0.7452$, $c_9 = -0.1302$.

$$Bo = \frac{q_i}{g_i r_0} \tag{12}$$

$$X_{tt} = \left(\frac{1-\overline{x}}{\overline{x}}\right)^{0.9}\left(\frac{\rho_G}{\rho_L}\right)^{0.5}\left(\frac{\mu_L}{\mu_G}\right)^{0.1} \tag{13}$$

where, q_i is the heat flux; g_i is the unit mass velocity; $\overline{x}$ is the average dryness; d_i is the inner diameter of the tube; P_0 is the evaporating pressure; ρ_L, ρ_G is the liquid and vapor density; μ_L, μ_G is the liquid and vapor

dynamic viscosity; σ is the surface tension; r_0 is the latent heat of evaporation; δ/f is the liquid thickness and fin height ratio, usually regarded as 1; Pr_L is the liquid Planter number; Re_L is the liquid Reynolds number; α_L is the liquid convective heat transfer coefficient, λ_L is Liquid thermal conductivity, W/(m·s).

2.1.3 Calculation of Heat Exchange and Tube Wall Temperature

When calculating the heat exchange, the air inlet state, the air volume, the dryness of the refrigerant inlet and outlet, and the structural parameters of the fin and the single tube of the heat exchanger are known. The parameters to be assumed include heat exchange Q_0 and tube wall temperature t_w.

The difference in specific enthalpy between inlet and outlet air is Eq. (14) [21]

$$\Delta h = \frac{Q_0 v_1}{q_{va}} \tag{14}$$

where, Q_0 is the assumed heat exchange; v_1 is the specific volume of wet air; q_{va} is the Air volume flow rate of air.

The enthalpy h_w and the humidity value d_w at a relative humidity of $\varphi_w = 100\%$ are found for the wall temperature t_w. The saturation point of the air is determined. The enthalpy and humidity diagram are then used to determine the average air inlet and outlet temperature and state parameter.

The heat transfer coefficient based on the area outside the tube is Eq. (15) [22]

$$K_0 = \frac{1}{\frac{\beta}{\alpha_i} + R + \frac{1}{\alpha_j}} \tag{15}$$

where, β is the Ribification coefficient; R is the sum of the thermal resistance to external fouling, the contact thermal resistance, and the thermal resistance to thermal conductivity, $(\mathrm{m}^2\cdot\mathrm{K})/\mathrm{W}$; α_i is the heat transfer coefficient on the inner side of the tube, $\mathrm{W}/(\mathrm{m}^2\cdot\mathrm{K})$; α_j is the air-side equivalent surface heat transfer coefficient, $\mathrm{W}/(\mathrm{m}^2\cdot\mathrm{K})$.

The calibrated heat exchange is Eq. (16) [23]:

$$Q_0^{'} = \beta K_o A_i \Delta T_m \tag{16}$$

The inner wall temperature of the tube is Eq. (17):

$$T_i = \frac{\beta K_o \Delta T_m}{\alpha_i} + T_s \tag{17}$$

The outer wall temperature of the tube is Eq. (18):

$$T_w^{'} = \frac{Q_0^{'}}{2\pi\lambda l} \ln \frac{d_o}{d_i} + T_i \tag{18}$$

where, λ is the thermal conductivity of the copper tube; l is the length of the tube, m; ΔT_m is the logarithmic mean heat transfer temperature difference.

In the numerical computation, Q_0 and T_w are adopted as the initial guessed values of heat exchange level and outer tube wall temperature. Iterative computation is then performed to derive the updated $Q_0^{'}$ and $T_w^{'}$ corresponding to the heat exchange performance and tube wall temperature, respectively. Subsequently, the newly solved data are compared with the initially presumed parameters. A relative error below 1%

signifies that the updated $Q_0^{'}$ and $T_w^{'}$ can be adopted as the authentic computational results. If the error exceeds this threshold, the initial presumed parameters will be reset, and the entire iterative procedure will be executed repeatedly until the convergence criterion is satisfied.

The aforementioned calculation formula is based on the assumption that air enters the tube bundle along the vertical axis of the tubes with uniform velocity distribution. In actual indoor units, however, air flow is chaotic and non-uniform. Consequently, discrepancies between theoretical calculations and practical conditions may occur, but subsequent validation confirms these deviations remain within acceptable limits. Therefore, the theoretical calculation method can serve as an analytical tool for tube bundle heat transfer in indoor units.

2.2 Calculation of Refrigerant Pressure Drop in the Tube of the Indoor Unit

Refrigerant circulates steadily inside the tube passages of the heat exchanger. During the boiling heat transfer process, the refrigerant gradually increases in dryness fraction, which raises the flow resistance and induces a noticeable pressure drop. This pressure variation further alters the saturation evaporation temperature of the refrigerant. A deviation in evaporation temperature can be observed between the inlet and outlet sections of the heat exchanger. On this basis, taking the outlet temperature of the refrigerant as the starting condition, iterative computation combining pressure drop and evaporating temperature is adopted to obtain the fluctuation range of the refrigerant evaporating temperature.

2.2.1 Calculation of Pressure Drop in a Single Diameter Tube

The frictional pressure drop of the refrigerant in the tube is calculated using the Chisholm formula Eq. (19) [24]:

$$\frac{dF}{dZ} = \Phi_{LO}^2 \left(\frac{dF}{dZ}\right)_{LO} \tag{19}$$

where, d_F/d_Z is the pressure drop gradient for two-phase flow, ϕ_{LO}^2 is the two-phase flow factor at total flow rate calculated by liquid properties, $(d_F/d_Z)_{LO}$ is the pressure drop gradient calculated by liquid phase.

The total pressure drop in the tube is calculated as Eq. (20):

$$\Delta P = \frac{dF}{dZ} NL \tag{20}$$

where, N is the number of flows; L is the length of a single tube.

2.2.2 Pressure Drop at Tube Diameter Burst

To address the pressure characteristics of gas–liquid two-phase refrigerant flow through a sudden tube expansion, Schmidt and Friedel [25] proposed a theoretical model incorporating the effect of liquid entrainment. This model can be applied to quantify the pressure variation occurring at the junction of pipelines with different diameters, and the corresponding pressure change can be calculated via Eq. (21).

$$\Delta P = \frac{\hat{m}_2^2 \left[\frac{\sigma_{2,3}}{\rho_{eff,2}} - \frac{\sigma_{2,3}^2}{\rho_{eff,3}} - f_{Exp} \rho_{eff,2} \left(\frac{\widehat{x}}{\rho_{g,2} \varepsilon_2} - \frac{1-\widehat{x}}{\rho_{g,2}(1-\varepsilon_2)} \right)^2 \left(1 - \sqrt{\sigma_{2,3}}\right)^2 \right]}{1 - \Gamma_{Exp}(1 - \sigma_{2,3})} \tag{21}$$

where,

$$\frac{1}{\rho_{eff}} = \frac{\widehat{x}}{\rho_g \varepsilon} + \frac{(1-\widehat{x})^2}{\rho_l(1-\varepsilon)} + \rho_l(1-\varepsilon)\left(\frac{\varepsilon_E}{1-\varepsilon_E}\right)\left[\frac{\widehat{x}}{\rho_g \varepsilon} - \frac{1-\widehat{x}}{\rho_l(1-\varepsilon)}\right]^2 \tag{22}$$

$$\Gamma_{Exp} = 1 - \sigma_{2,3}^{0.25} \tag{23}$$

where, ρ_l is the density of the saturated liquid; ε, ε_E are the empirical coefficient; $\hat{m}_2$ is the refrigerant mass flow rate in a small diameter heat exchanger tube. $\sigma_{2,3}$ is the ratio of the cross-sectional area of the flow of the small and large diameter heat exchanger tubes with d_2, d_3 as the diameter. $\widehat{x}$ is the dryness of two-phase fluid mixture.

2.3 Comparison of Theoretical Calculated Values and Experimental Data for Indoor Units at Rated Cooling Condition

In light of the SAC indoor unit performance experiments utilizing a 7.3 mm tube diameter, R32 refrigerant was selected for the trial. Table 1 displays the rated refrigeration operating condition for both theoretical calculations and experimental data. With a mere 4.33% error between the calculated and measured latent heat, and a 0.7% error between the calculated pressure drop and measured refrigerant pressure drop, it is evident that the theoretical correlation calculation holds a degree of reliability.

Table 1: Comparison of experimental data and theoretical calculated values under rated refrigeration working conditions.

	Air Inlet Dry/Wet Bulb Temperature/°C	The Outer Wall Temperature of the Heat Exchanger Heat Exchange Tube/°C	Refrigerant Inlet Temperature/°C	Refrigerant Outlet Temperature/°C	Pressure Drop in Tube/kPa	The Latente Heat of the Air Outside the Heat Exchanger Tube/W	The Sensible Heat of the Air Outside the Heat Exchanger Tube/W	The Total Heat of the Air Outside the Heat Exchanger Tube/W
experimental value	27/19	\	9.48	8.78	22.80	393	3065	3458
Theoretical and simulated values	27/19	12.1	\	\	22.96	410	2978	3388
error	\	\	\	\	0.07%	4.33%	2.8%	3.4%

3 Numerical Approach

3.1 Physical Model

The physical model of the Split Air Conditioner (SAC) indoor unit, as provided by the manufacturer, is shown in Fig. 4a. To simplify the physical model and reduce the computational cost associated with its intricate geometry, the periodic structure of the fins is considered. The computational domain is thus defined as the region between two adjacent fins, incorporating the fin thickness and the inter-fin spacing. Furthermore, components such as the condensate pan, air filter, and other auxiliary parts are considered to have a negligible effect on the indoor unit's thermal performance and are therefore omitted from the model. Consequently, the physical model is simplified to the configuration shown in Fig. 4b, which includes heat exchange tubes with an outer diameter of 7.3 mm. The dimensions of the simplified model are 300 mm in height, 200 mm in width, and 2.6 mm in depth (covering the region of two fins).

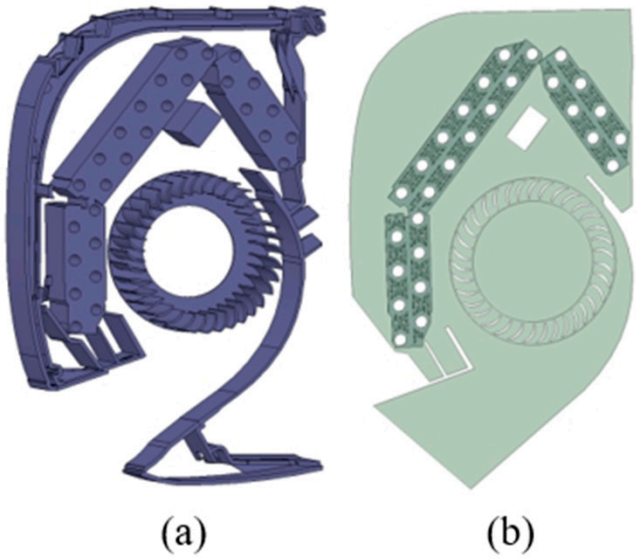

Figure 4: Physical model of split air conditioning indoor unit (**a**) 3D structural diagram of indoor unit (**b**) Simplified model of indoor unit.

This article presents three different combinations of variable tube diameter heat exchange, based on the SAC indoor unit structure (Fig. 1). As depicted in Table 2, the proposed combinations are referred to as Case 1, Case 2, and Case 3, with Case 0 serving as the reference point for tube diameter (7.3 mm). These variable tube diameter combination schemes have been developed to enhance the functionality of the indoor unit structure and improve overall performance.

Table 2: Variable tube diameter combination scheme.

	Heat Exchange Tube Diameter/mm		Number of Heat Exchange Tubes/pc		Tube Pitch/mm	
	A Tube Sheet	B Tube Sheet	A Tube Sheet	B Tube Sheet	A Tube Sheet	B Tube Sheet
Case 0	7.3	7.3	8	20	21	21
Case 1	5.2	7.3	10	20	17.5	21
Case 2	5.2	7.3	12	20	14	21
Case 3	5.2	7.3	14	18	15	21

As illustrated in Fig. 5, variable tube diameter heat exchangers are designed with two distinct flow paths for different pipe diameters. The area division and refrigerant flow path are divided accordingly, with the refrigerant passing through both paths from inlet 1 to outlet 2. The A tube sheet is the first point of passage, followed by the B tube sheet.

As shown in Fig. 6, the variable tube diameter heat exchanger adopts sleeve-type fins, with outer diameters of 7.3 mm and 5.2 mm respectively, located at the circular position in the fins; The fins are slotted, and the types and parameters of fins used in heat exchangers with different pipe diameters are different. The fin parameters are shown in Table 3; The diameter of the rotating area of the fan is close to the width of the impeller, with an outer diameter of 102 mm and an inner diameter of 74 mm.

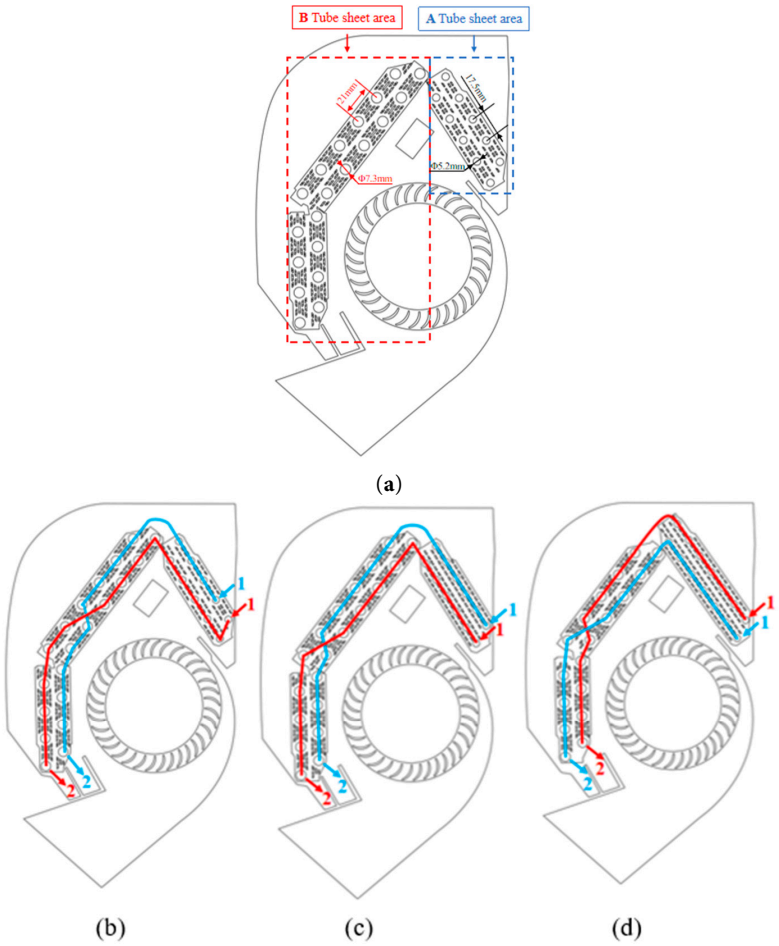

Figure 5: Division of Tube Plate Area and Refrigerant Flow Distribution Scheme for Variable Tube Diameter Heat Exchangers. (**a**) case 0; (**b**) case 1; (**c**) case 2; (**d**) case 3.

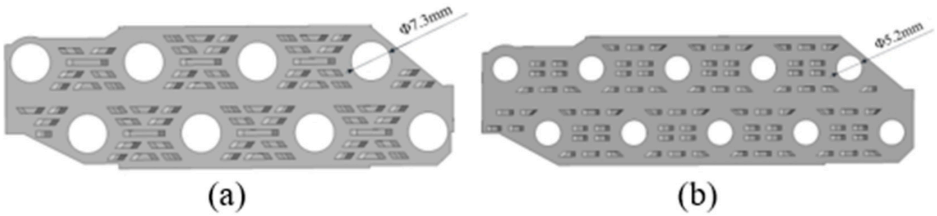

Figure 6: Fin shape and slot form of a set of finned variable tube diameter heat exchangers; (**a**) 7.3 mm, (**b**) 5.2 mm.

Table 3: Parameters of set of finned tube heat exchanger.

Fin-and-Tube Parameters	7.3 mm Heat Exchanger Tube	5.2 mm Heat Exchanger Tube
Base tube outer diameter do/mm	7.3	5.2
Base tube inner diameter di/mm	6.5	4.54
Transverse tube pitch s1/mm	21	17.5
Longitudinal tube pitch s2/mm	13.3	13.3
Slit height h/mm	0.65	0.5
Fin thickness δ/mm	0.095	0.095
Fin pitch f/mm	1.3	1.3

3.2 Grid Division and Dynamic and Static Area Processing

In this study, the preprocessing software Fluent Meshing (Fluent 2020R2) was used to generate the mesh for the indoor unit of the air conditioner, including components such as internal fins, fans, and impellers. This software supports the generation of poly-hexcore meshes (Poly Hexcore), which offer the advantage of achieving a reduced cell count while maintaining high mesh quality, thereby facilitating favorable convergence behavior during computation. Given the complexity of the indoor unit system, mesh refinement was applied in multiple regions to ensure computational accuracy. As illustrated in Fig. 7, certain regions of the fan impeller undergo rotational motion, necessitating a high mesh resolution in these moving zones for accurate simulation. Accordingly, the impeller rotation zone and the internal fan region were densely meshed. As depicted in Fig. 8, the mesh of the finned tube was refined due to the presence of solid-to-solid heat conduction, air-to-fin surface convective heat transfer, and the thinness and dense slit structure of the fins—all of which impose stringent requirements on mesh quality and density in this region. Furthermore, to ensure the accuracy of subsequent simulation results for the indoor unit, three-layer boundary layer meshes were applied in regions characterized by velocity boundary layers, such as the wall surfaces and impeller surfaces, as shown in Fig. 9.

The rotation of the fan impeller drives airflow into and out of the indoor unit, as illustrated in Fig. 7. Consequently, the indoor unit was divided into three key zones: the heat exchange zone, the impeller rotation zone, and the fan inner circle zone. During operation, the impeller rotation zone rotates at a constant speed, representing the dynamic region, while the heat exchange zone and the fan inner circle zone remain stationary, constituting the static regions. In numerical simulations, the coupling between dynamic and static regions is a critical issue that requires careful handling. This study primarily investigates heat transfer using a steady flow configuration. The moving reference frame (MRF) model was applied to handle the impeller rotation zone, with Frame Motion specified for the impeller rotation zone and a Moving Wall boundary condition assigned to the impeller wall to maintain relative stability with the rotating impeller region. To facilitate data transfer between the dynamic and static regions, interface pairs were employed. An interface consists of two overlapping interface surfaces, as shown in Fig. 7. In the model used in this study, which comprises two static regions and one dynamic region, two interfaces were established, located at the outer and inner circles of the impeller rotation zone.

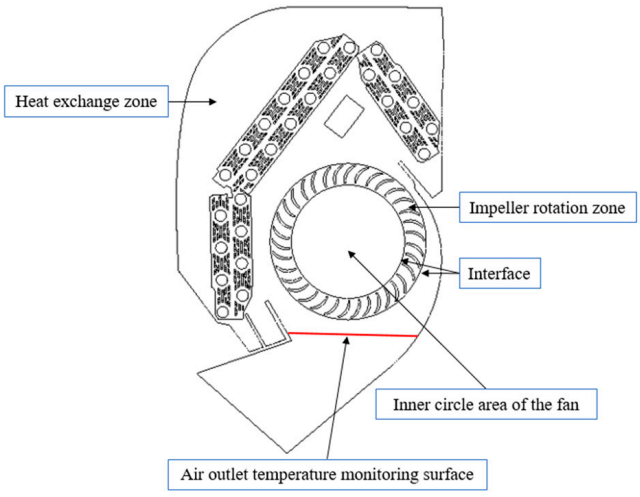

Figure 7: Indoor unit model area division.

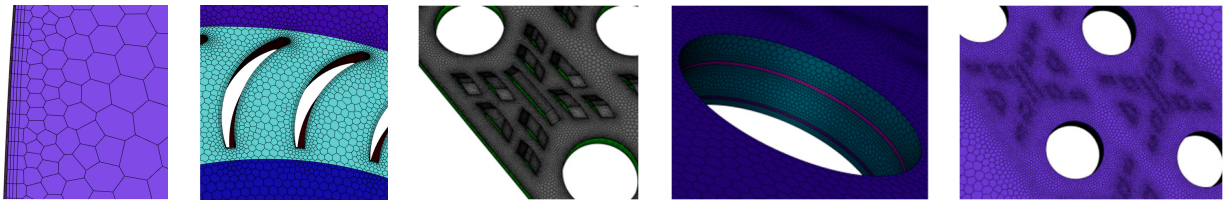

Figure 8: Localized mesh encryption for each boundary layer (**a**) Grid for wall boundary layer (**b**) Blade boundary layer mesh (**c**) Grid densification at slit details (**d**) Heat exchange tube details with grid densification (**e**) Grid refinement at the slit details in the fluid domain.

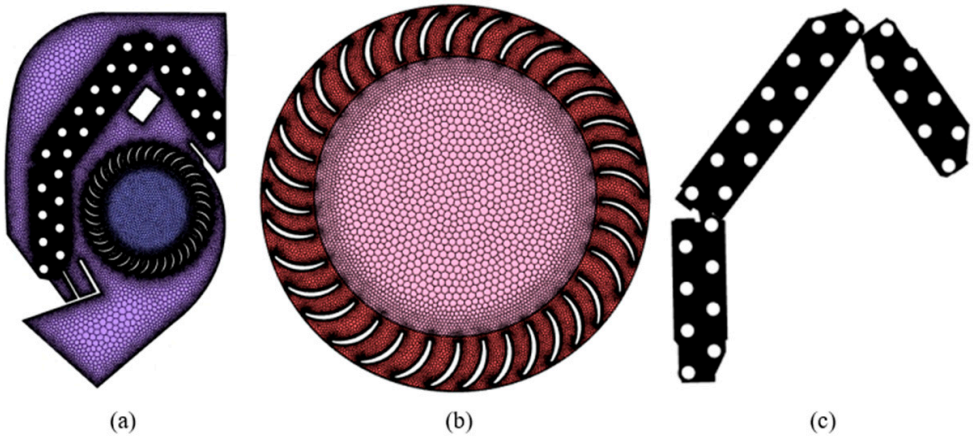

Figure 9: Overall grid encryption of indoor unit (**a**) cross-flow fan (**b**) and fins (**c**).

3.3 Boundary Condition and Numerical Strategies

Boundary conditions refer to the prescribed patterns of spatial and temporal variations for variables that need to be solved at the boundaries of the solution domain. Pressure inlet conditions are utilized to define the total pressure at the flow inlet boundary and are applicable when the inlet pressure conditions are known. In this study, as illustrated in Fig. 10, a pressure inlet boundary condition is applied at the inlet of the indoor unit, with the total pressure value estimated based on atmospheric pressure. A pressure outlet boundary condition is employed at the outlet, which is suitable for cases where the static pressure is unknown and must be determined by the internal flow field and boundary conditions. This approach accommodates scenarios in which both the outlet flow rate and velocity are unknown. As shown in Fig. 10, the outlet condition can also address cases with unspecified outlet flow and velocity conditions. However, it is incompatible with models that adopt the pressure inlet condition at the inlet. Therefore, the pressure outlet condition is selected as the exit boundary condition in this study. Compared to the output condition, the pressure outlet condition is susceptible to backflow at the outlet. Nevertheless, for the heat transfer model investigated in this study, the primary focus is on the heat transfer characteristics of the finned tube, as depicted in Fig. 7. The outlet air temperature after heat exchange with the finned tube is obtained from a cross-section located 5 mm below the fan. Thus, the backflow phenomenon does not affect the heat transfer behavior examined in this model. Accordingly, the use of the pressure outlet condition is justified. The detailed boundary conditions are summarized in Table 4.

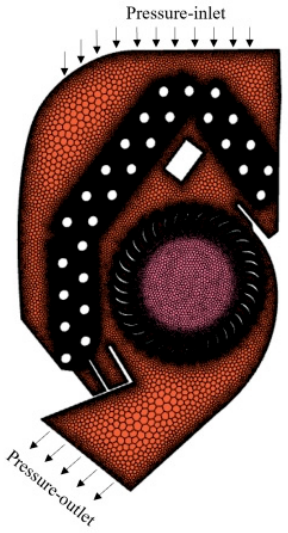

Figure 10: Input and output boundary conditions.

Table 4: Boundary condition setting.

Boundary Condition	Boundary Type	Boundary Value
Inlet condition	Pressure-inlet	101, 325 Pa
Outlet condition	Pressure-outlet	101, 325 Pa
Cross-flow fan	Rotation domain (MRF)	1700, 1413, 1506, 1768 r/min
The outer wall temperature of the heat exchanger heat exchange tube	Constant	10.5, 17.9, 12.1, 19.7°C

The wall condition is employed to specify the initial condition of the wall surface. In this study, it is assumed that each wall behaves as a non-slip boundary. The heat exchange tube wall is assigned a fixed temperature, while the remaining walls adopt adiabatic wall conditions. The periodic condition is utilized to define the boundaries of a periodic computational domain where both flow and heat transfer exhibit periodic repetition. As the model in this study simulates and calculates a section of the indoor unit with a radial thickness of 2.6 mm, including two fins, the front and rear walls of the model adopt periodic conditions due to the periodic distribution of fins.

In summary, this paper conducts simulations of three-dimensional, steady, incompressible fluid flow and heat transfer. A pressure-based solver is selected, along with the Standard k-ε turbulence model. The SIMPLE algorithm is applied for pressure-velocity coupling. The control equations for momentum, turbulent kinetic energy, and turbulent dissipation rate are discretized using the second-order upwind scheme. Furthermore, the physical parameters of the refrigerants utilized in subsequent calculations are obtained from Refprop9.1 software.

3.4 Governing Equations

Based on the actual operating conditions of the SAC indoor unit, several assumptions are made for the simulation: (1) Radiation heat transfer is neglected; (2) Air velocity and pressure differences are low, and density changes are negligible. Therefore, air is treated as an incompressible fluid with constant physical properties; (3) The model wall is assigned a non-slip boundary condition; (4) Thermal resistance due to dirt accumulation is ignored; (5) Contact thermal resistance between the fins and tube wall is neglected, and the temperature at the root of the fins is assumed to be equal to that of the tube wall.

The airflow and heat transfer process is governed by the continuity, momentum, and energy equations. The mathematical representation of fluid motion through these conservation laws constitutes the Navier-Stokes equations, which serve as the fundamental control equations in fluid dynamics. While the mass and momentum conservation laws suffice for solving flow problems in ordinary fluids, for comprehensive heat transfer problems involving both conduction and convection (i.e., flow-heat transfer coupling problems), the energy equation must be included to obtain a complete solution to the problem.

(1) Continuity equation

The equation of continuity, based on the law of conservation of mass and using the micro-element assumption is Eq. (24):

$$\frac{\partial u}{\partial x}+\frac{\partial v}{\partial y}+\frac{\partial w}{\partial z}=0 \tag{24}$$

where, u, v, w are the velocity components in the direction of x, y, z respectively, m/s.

(2) Momentum equation

Based on the conservation of momentum principle, the differential form of the conservation of momentum equation is obtained by establishing the momentum equation using the micro-element assumption and introducing the concept of tensor.

$$\begin{aligned}&\frac{\partial(\rho\overline{u})}{\partial t}+\frac{\partial(\rho\overline{uu})}{\partial x}+\frac{\partial(\rho\overline{uv})}{\partial y}+\frac{\partial(\rho\overline{uw})}{\partial z}=-\frac{\partial\overline{P}}{\partial x}+\frac{\partial\overline{\tau}_{xx}}{\partial x}+\frac{\partial\overline{\tau}_{yx}}{\partial y}+\frac{\partial\overline{\tau}_{zx}}{\partial z}\\&+\frac{\partial\left(-\rho\overline{u'^2}\right)}{\partial x}+\frac{\partial\left(-\rho\overline{u'v'}\right)}{\partial y}+\frac{\partial\left(-\rho\overline{u'w'}\right)}{\partial z}+F_x\end{aligned} \tag{25}$$

$$\begin{aligned}&\frac{\partial(\rho\overline{v})}{\partial t}+\frac{\partial(\rho\overline{vu})}{\partial x}+\frac{\partial(\rho\overline{vv})}{\partial y}+\frac{\partial(\rho\overline{vw})}{\partial z}=-\frac{\partial\overline{P}}{\partial y}+\frac{\partial\overline{\tau}_{xy}}{\partial x}+\frac{\partial\overline{\tau}_{yy}}{\partial y}+\frac{\partial\overline{\tau}_{zy}}{\partial z}\\&+\frac{\partial\left(-\rho\overline{v'u'}\right)}{\partial x}+\frac{\partial\left(-\rho\overline{v'^2}\right)}{\partial y}+\frac{\partial\left(-\rho\overline{v'w'}\right)}{\partial z}+F_y\end{aligned} \tag{26}$$

$$\begin{aligned}&\frac{\partial(\rho w)}{\partial t}+\frac{\partial(\rho\overline{wu})}{\partial x}+\frac{\partial(\rho\overline{wv})}{\partial y}+\frac{\partial(\rho\overline{ww})}{\partial z}=-\frac{\partial\overline{P}}{\partial z}+\frac{\partial\overline{\tau}_{xz}}{\partial x}+\frac{\partial\overline{\tau}_{yz}}{\partial y}+\frac{\partial\overline{\tau}_{zz}}{\partial z}\\&+\frac{\partial\left(-\rho\overline{w'u'}\right)}{\partial x}+\frac{\partial\left(-\rho\overline{w'v'}\right)}{\partial y}+\frac{\partial\left(-\rho\overline{w'^2}\right)}{\partial z}+F_z\end{aligned} \tag{27}$$

where P is the pressure, Pa; τ_{xx}, τ_{xy}, τ_{xz} is the viscous stress fraction, Pa; $F_x=0$, $F_y=0$, $F_z=-\rho g$ is the volume force, N.

(3) Energy equation

The differential form of the conservation of energy equation is Eq. (28):

$$\frac{\partial\left(\rho\overline{T}\right)}{\partial T}+\frac{\partial\left(\rho\overline{u}\overline{T}\right)}{\partial x}+\frac{\partial\left(\rho\overline{u}\overline{T}\right)}{\partial y}+\frac{\partial\left(\rho\overline{u}\overline{T}\right)}{\partial z}=\frac{\partial}{\partial x}\left(\frac{\kappa}{c_p}\frac{\partial\overline{T}}{\partial x}\right)+\frac{\partial}{\partial y}\left(\frac{\kappa}{c_p}\frac{\partial\overline{T}}{\partial y}\right)+\frac{\partial}{\partial z}\left(\frac{\kappa}{c_p}\frac{\partial\overline{T}}{\partial z}\right) \tag{28}$$

where T is the thermodynamic temperature, c_p is the specific heat capacity, κ is the heat transfer coefficient of the fluid.

For the specific problem of indoor fan rotation driving air flow and heat transfer studied in this article, Standard k from the two-equation turbulence model is selected-ε. The model is used for calculation, which includes the turbulent kinetic energy equation and the dissipation rate equation. The model equation will be described in detail below.

Average velocity:

$$\overline{u}_i = \frac{1}{\Delta t}\int_t^{t+\Delta t} u_i(t)dt \tag{29}$$

Velocity fluctuations:

$$u'_i = u_i - \overline{u}_i \tag{30}$$

Turbulent kinetic energy:

$$\kappa = \frac{1}{2}\left(\overline{u'^2} + \overline{v'^2} + \overline{w'^2}\right) \tag{31}$$

where, u', v' and w' are the velocity components in the directions of, x, y and z, respectively, m/s.

Turbulent energy dissipation rate:

$$\varepsilon = \overline{\frac{\mu}{\rho}\left(\frac{\partial u'_i}{\partial x_\kappa} + \frac{\partial u'_j}{\partial x_\kappa}\right)} \tag{32}$$

the turbulent kinetic viscosity:

$$\mu_t = \rho C_\mu \frac{\kappa^2}{\varepsilon} \tag{33}$$

The turbulent kinetic viscosity is used to evaluate the turbulent Reynolds stresses appearing at the right-hand side of Eqs. (25)–(27). where, C_μ is the empirical constant, often taken as 0.09.

$$G_\kappa = \mu_t\left(\frac{\partial \overline{u}_i}{\partial x_j} + \frac{\partial \overline{u}_j}{\partial x_i}\right)\frac{\partial \overline{u}_i}{\partial x_j} \tag{34}$$

In the Standard k-ε model, the values of the model constant $C_{1\varepsilon}, C_{2\varepsilon}, C_{3\varepsilon}, \sigma_\kappa, \sigma_\varepsilon$ are $C_{1\varepsilon} = 1.44$, $C_{2\varepsilon} = 1.92$, $C_{3\varepsilon} = 0.09$, $\sigma_\kappa = 1.0$, $\sigma_\varepsilon = 1.3$, respectively.

When incompressible fluid flows and user-defined source terms are not considered $G_b = 0$, $Y_M = 0$, $S_K = 0$, $S_\varepsilon = 0$, The Standard k-ε is:

$$\frac{\partial(\rho\overline{\kappa})}{\partial t} + \frac{\partial(\rho\overline{\kappa}u_i)}{\partial x_i} = \frac{\partial}{\partial x_j}\left[\left(\mu + \frac{\mu_t}{\sigma_\kappa}\right)\frac{\partial \overline{\kappa}}{\partial x_j}\right] + G_\kappa - \rho\overline{\varepsilon} \tag{35}$$

$$\frac{\partial(\rho\overline{\varepsilon})}{\partial t} + \frac{\partial(\rho\overline{\varepsilon}\,\overline{u}_i)}{\partial x_i} = \frac{\partial}{\partial x_j}\left[\left(\mu + \frac{\mu_t}{\sigma_\varepsilon}\right)\frac{\partial \overline{\varepsilon}}{\partial x_j}\right] + \frac{C_{1\varepsilon}\overline{\varepsilon}}{\overline{\kappa}} - C_{2\varepsilon}\rho\frac{\overline{\varepsilon}^2}{\overline{\kappa}} \tag{36}$$

3.5 Mesh Independence Check

The accuracy of numerical simulation calculations is closely linked to both the quality and quantity of the computational grid. To ensure accuracy in physical models with complex structures, mesh refinement

in the complex regions is often required, which increases the number of meshes. However, once the grid quality meets the required accuracy, further refinement will only increase computational load without improving calculation accuracy. For the present study, a grid independence verification was performed to determine the optimal number of grids for the physical model.

Five sets of grids ranging from 6.1 million to 10.1 million were chosen, and numerical simulations were conducted on indoor unit models with heat exchange tubes of 7 mm outer diameter (7.3 mm after expansion) under the specified boundary conditions. The computational results are presented in Fig. 11. Comparison shows that the difference in heat exchange between grids of 9 million and 10.1 million is less than 0.2%, indicating that 9 million can be regarded as an independent solution for the number of grids. Thus, to balance computational speed and accuracy, subsequent simulations will use a grid size of 9 million.

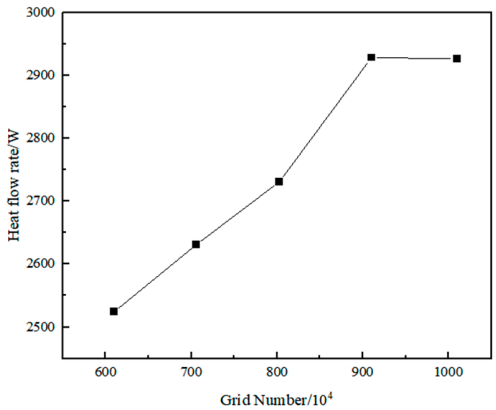

Figure 11: Relationship between simulated heat transfer and grid quantity.

3.6 Experimental Verification

3.6.1 Experimental Environment and Equipment

A standardized air enthalpy difference laboratory was employed to conduct this experiment, which aimed at a precise evaluation of the thermal performance of an indoor air conditioner heat exchanger. The laboratory configuration includes thermally insulated indoor and outdoor chambers, facilitating independent and precise climatic control on each side. The indoor unit, featuring a 7.3 mm diameter, was installed in the indoor side room. Heat transfer tests were conducted on air conditioners to measure performance parameters, including air temperature, humidity, and airflow volume. The laboratory comprises several essential systems: the air conditioning and processing systems, temperature and humidity sampling systems, air volume measurement systems, electrical control systems, and calculation and measurement systems. The temperature and humidity sampling system provides measurements of dry-bulb temperature and wet-bulb temperature, while Vane anemometer measures the air volume flow rate. The refrigerant temperature is obtained by a thermal resistance thermometer embedded in the pipeline. By utilizing an enthalpy humidity chart, the enthalpy values of the air at each point can be determined to calculate heat transfer (cooling capacity). Due to the influence of equipment accuracy, measurement method and other factors, the measurement data inevitably have experimental uncertainty; therefore, the uncertainty analysis is conducted. The directly measured uncertainties are presented in Table 5. The uncertainty of different variables in this experiment can be calculated from formula 37 (Moffat, 1988) [26]. Therefore, the uncertainty of the heat change is 5.76%.

$$uR = \left[\sum_{i=1}^{N}\left(\frac{\partial R}{\partial xi}\right)^{2} u^{2}(xi)\right]^{\frac{1}{2}} \tag{37}$$

Table 5: Summary of experimental uncertainties.

Name	Range	Unit	Measuring Instrument	Precision	Uncertainty
Air temperature and humidity	233–398 0–100%RH	K	Temperature and humidity sensor	±0.3 K ±2%	±0.17 ±0.01
refrigerant temperature	223–473	K	Platinum resistance thermometer	±0.15 K	±0.08
Pressure	0–5	MPa	Pressure sensor	±0.015 MPa	±0.008
Air Volume Flow Rate	0–1550	m^3/h	Vane anemometer	±0.1 m/s	±0.06
Power	0.1–5	kW	Dynamometer	±0.01 kW	±0.006

3.6.2 Experimental Data

The air volume and heat transfer of a 7.3 mm tube diameter heat exchanger under four operating conditions of low temperature rated refrigeration, low temperature intermediate refrigeration, intermediate refrigeration, and rated refrigeration were measured through experiments, as shown in Table 6.

Table 6: Experimental data of 7.3 mm tube diameter heat exchange under cold working conditions of split air conditioning indoor.

	Low Temperature Rated Refrigeration	Low Temperature Intermediate Refrigeration	Rated Refrigeration	Intermediate Refrigeration
The average evaporation temperature of the refrigerant in the heat exchanger tube/°C	7.75	15.33	9.13	16.86
Cross-flow fan speed/(r/min)	1700	1413	1506	1768
Air Volume Flow Rate/(m^3/h)	910	728	825	950
The sensible heat of the air outside the heat exchanger tube/W	3193	1758	3065	1713
The latente heat of the air outside the heat exchanger tube/W	378	0	393	0
The Total heat of the air outside the heat exchanger tube/W	3571	1758	3458	1713

3.6.3 Simulation Calculation and Simulation Reliability Verification of 7.3 mm Diameter Heat Exchanger

Based on the experimental data of evaporation temperature and heat transfer inside the tube, the theoretical correlation calculation method in the previous section can be used to calculate the tube wall temperature. Then, the simulation calculation method in this section is used to simulate the convective heat transfer outside the heat exchange tube using indoor units with a diameter of 7.3 mm under different working conditions. The calculation results are shown in Table 7.

Table 7: Simulation calculation results of air side for indoor units with all 7.3 mm heat exchanger tubes under various working conditions.

	Low-Temperature-Rated Refrigeration	Low-Temperature Intermediate Refrigeration	Rated Refrigeration	Intermediate Refrigeration
The outer wall temperature of the heat exchanger heat exchange tube/°C	10.5	17.9	12.1	19.7
The sensible heat of the air outside the heat exchanger tube/W	3310	1678	2978	1624

Fig. 12 illustrates the comparison between the simulated data's sensible heat from Table 5 and the experimental data from Table 4. The maximum error between the simulation results and the experimental results is 3.24% (occurring at the operating point with an air volume of 910 m^3/h). It is important to note that errors are unavoidable due to the simplification of the physical model from the actual object as well as potential errors during the experimental process. Nevertheless, considering the small and acceptable error, it can be concluded that the numerical simulation model and parameter settings in this study possess a certain level of accuracy and reliability. Therefore, they can be utilized for subsequent optimization design calculations.

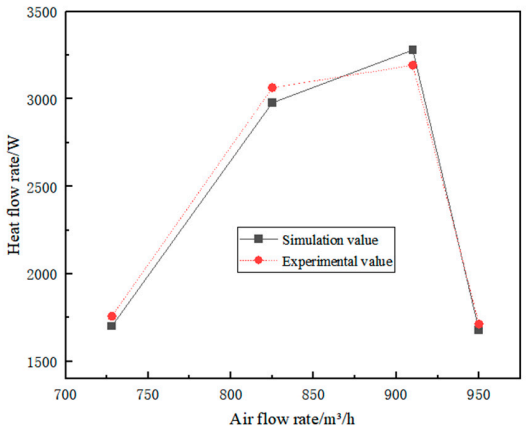

Figure 12: Comparison of heat transfer between experimental and simulated calculations.

4 Results and Discussions

This study investigates the heat transfer performance of a stand-alone air conditioner (SAC) indoor unit under rated cooling conditions using numerical simulations. The air-side heat transfer capacity was determined via computational fluid dynamics (CFD), while the refrigerant-side heat transfer and pressure drop in variable-diameter tubes were analyzed theoretically. A baseline case with a uniform tube diameter of 7.3 mm was also evaluated for comparison.

For consistency, all variable-diameter tube configurations were simulated using the same refrigerant outlet temperature and mass flow rate as the baseline. The system cooling capacity was subsequently derived, and the coefficient of performance (COP) was calculated based on a fixed compressor input power of 816 W. The simulation and theoretical results are summarized in Fig. 13a–d and Table 8.

Table 8: Calculation of performance coefficient (COP) based on fixed compressor input power.

	Total Heat Exchange on the Air Side/W	Input Power/W	COP
case 0	3271	816	4.01
case 1	3333.61	816	4.09
case 2	3393.52	816	4.16
case 3	3372.2	816	4.13

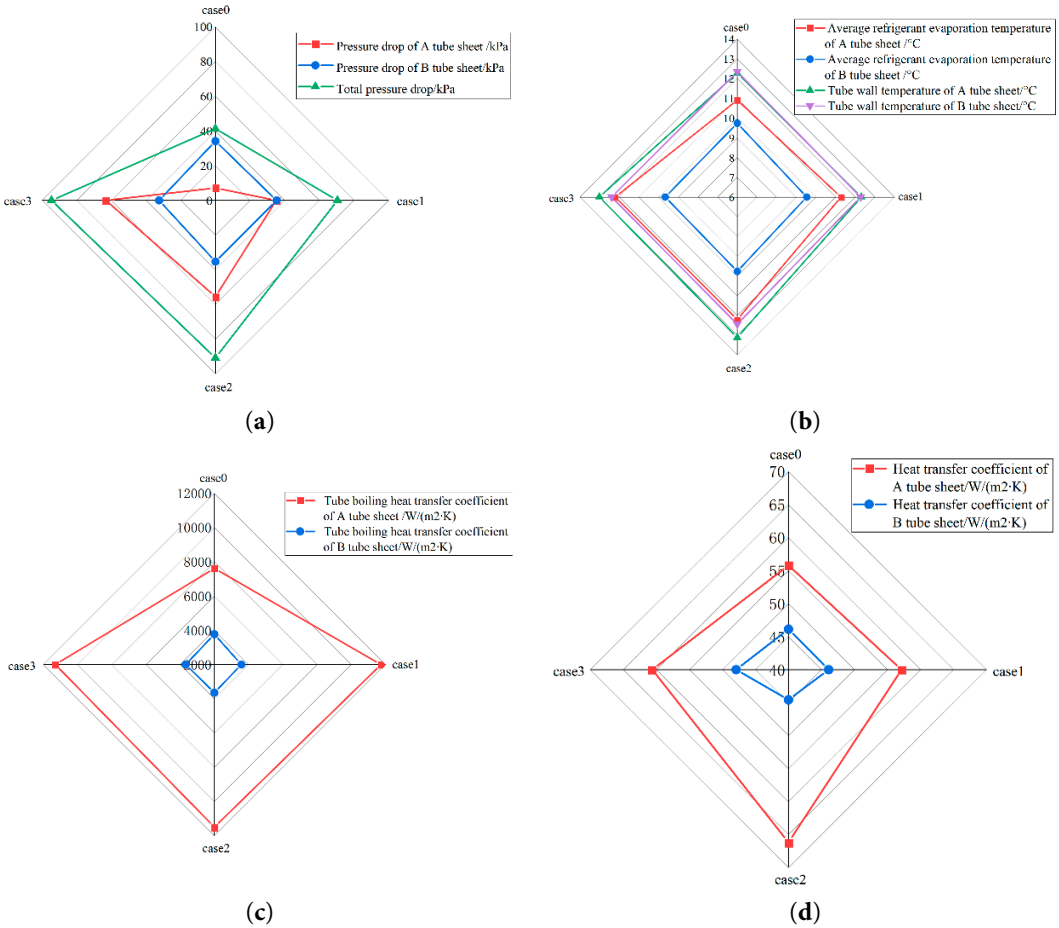

Figure 13: Simulation and theoretical calculation results of reference pipe diameter and variable tube diameter scheme under rated refrigeration conditions (**a**) pressure drop in the tube (**b**) average evaporation temperature and corresponding wall temperature of refrigerant in the tube (**c**) boiling heat transfer coefficient in the tube (**d**) Heat transfer coefficient.

4.1 Analysis of Heat Transfer and Flow Performance on the Air Side outside the Variable Tube Diameter Heat Exchanger

Figs. 14–16 present the air-side fin surface heat transfer coefficient, temperature distribution, and velocity vector fields for the baseline (Case 0) and three variable-diameter configurations (Cases 1–3).

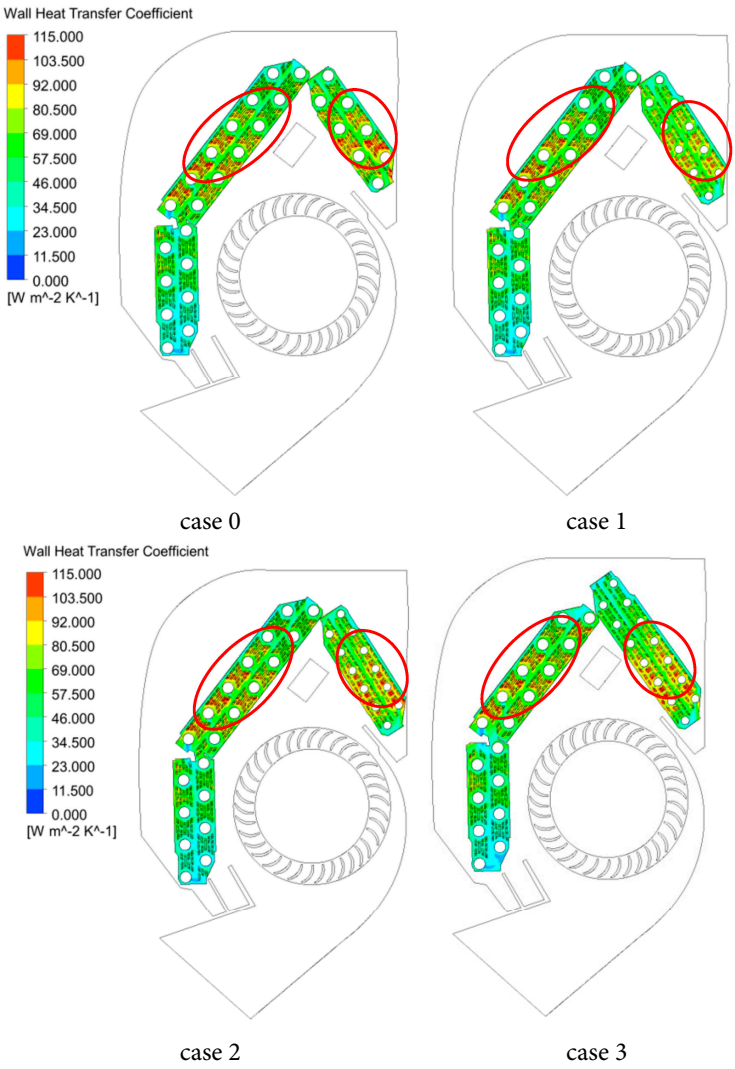

Figure 14: Distribution diagram of heat transfer coefficient on the air side fin surface of R290 reference rand variable tube diameter heat exchanger.

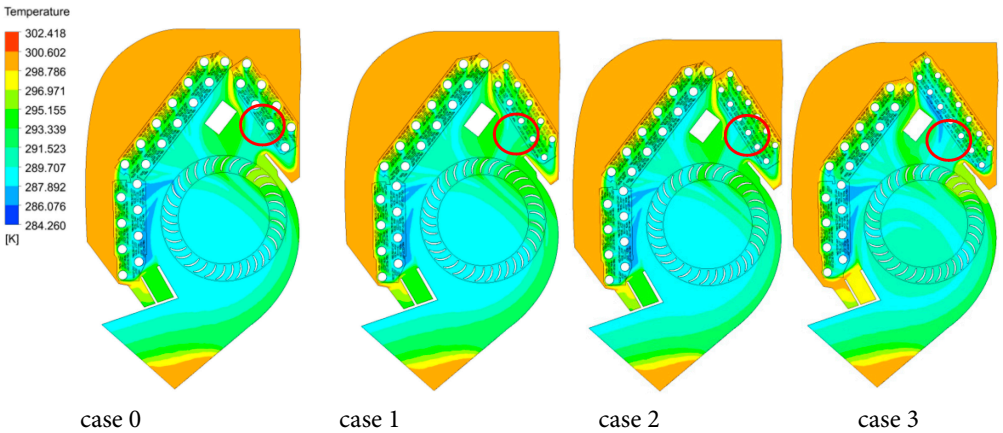

Figure 15: Air side temperature distribution diagram of R290 reference and variable tube diameter heat exchanger.

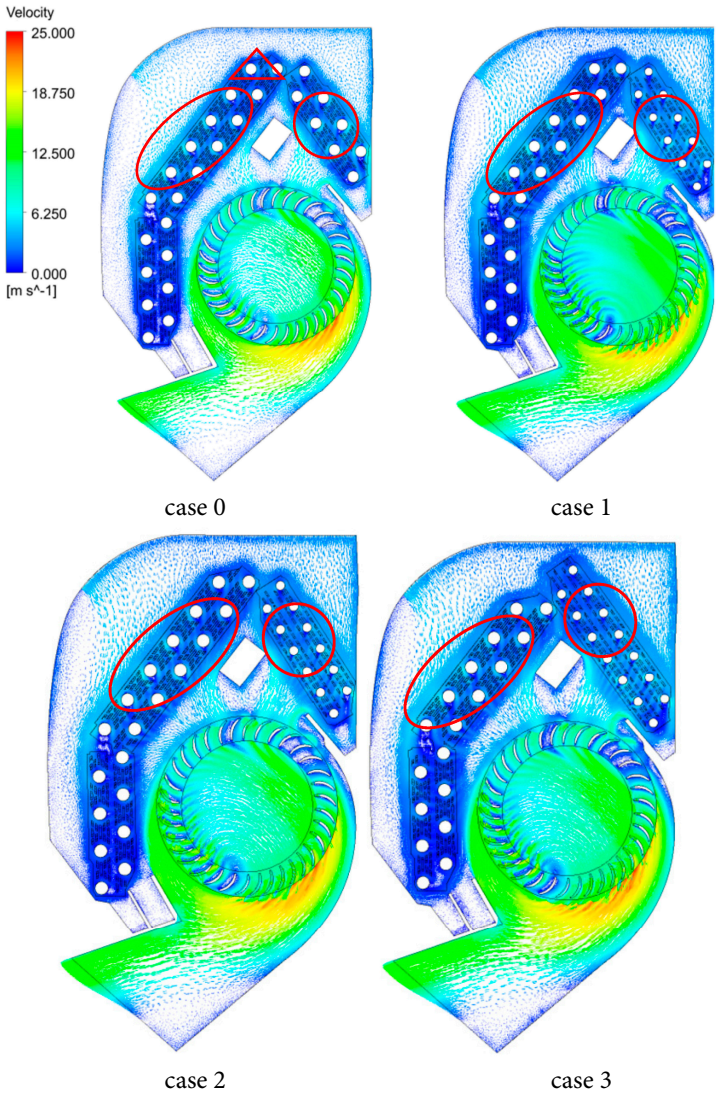

Figure 16: Air side Velocity Distribution Diagram of R290 reference and variable tube diameter heat exchanger.

As shown in Fig. 16, a region near the fan consistently exhibits elevated air velocity due to the unobstructed flow path, enhancing local convective heat transfer and fin efficiency. Conversely, the lower section of the B tube sheet experiences restricted inlet flow, resulting in lower air velocity.

In Case 1, the A tube sheet benefits from a relatively high airflow rate combined with a 3.67% increase in air-side surface area relative to Case 0, leading to a notable enhancement in air-side heat transfer. The highest fin surface heat transfer coefficients are concentrated in these high-velocity regions (Fig. 14). However, the reduction in tube diameter in the A sheet increases refrigerant-side pressure drop (Fig. 13a), raising the average evaporation temperature and, consequently, the tube wall temperature. This reduces the air-to-wall temperature difference—the driving potential for heat transfer—which alone would degrade performance. Nonetheless, the combined effect of increased airflow and extended surface area outweighs this penalty, yielding a net improvement over Case 0.

Analysis of Table 2 reveals significant differences in case 2 compared to case 1. Case 2 introduces two additional 5.3 mm tubes in the A tube sheet and reduces the tube pitch by 3.5 mm, increasing the total external heat transfer area by 3.29% compared to Case 0. The airflow through the A sheet is also higher.

Although the increased number of smaller-diameter tubes raises the wall temperature, the augmented air volume and total surface area compensate effectively, resulting in a net enhancement of heat exchanger efficiency. As shown in Figs. 13b and 14, the fin heat transfer coefficient in the lower A sheet region of Case 2 surpasses that of Case 1. Despite a slightly higher average wall temperature in the small-tube plate, the increased tube count and improved fin-side heat transfer coefficient render Case 2 superior overall.

In Case 3, the total external surface area increases by 3.62% relative to Case 0, although the area in the B tube sheet decreases by 11.05%. The design concentrates the largest number of 5.3 mm tubes in the A sheet—the region with the highest airflow—substantially improving its heat transfer performance. This is achieved by removing two 7.3 mm tubes from the low-airflow region of the B sheet (indicated by the red triangle in Fig. 16, Case 0) and adding two 5.2 mm tubes to the A sheet. While the removal reduces heat transfer area, the fins on those tubes exhibited low local heat transfer coefficients, minimizing the penalty. The new smaller tubes in the A sheet significantly enhance refrigerant-side boiling heat transfer, and the gain in the high-performance A sheet more than compensates for the loss in the low-performance B sheet region, resulting in a net efficiency improvement.

4.2 Analysis of Refrigerant Boiling Heat Transfer Performance in Variable Tube Diameter Heat Exchangers

Fig. 13a,c show that in Case 1, the boiling heat transfer coefficient in the A tube sheet increases by 54.05% relative to Case 0, while decreasing by 5.12% in the B sheet. In the A sheet, where the average refrigerant quality is low, nucleate boiling dominates. The reduced tube diameter increases the R290 flow velocity, promoting more vigorous bubble formation and departure. Bubbles are rapidly carried away from the wall, allowing continuous nucleation and significantly enhancing the in-tube boiling heat transfer coefficient. In the B sheet, the higher gas-phase fraction upon entry increases flow resistance and promotes early mist flow, elevating internal heat transfer resistance and suppressing boiling heat transfer. Nevertheless, the substantial enhancement in the A sheet yields an overall improvement.

Case 2 increases the boiling heat transfer coefficient by 50.88% in the A sheet and reduces it by only 3.4% in the B sheet compared to Case 0. The addition of two 5.3 mm tubes in the A sheet increases both the external heat transfer area and the R290 mass flow rate, intensifying bubble disturbance and nucleate boiling. In the B sheet, the higher gas-phase fraction and increased flow resistance lead to a reduced mass flow rate and convective heat transfer, lowering the boiling heat transfer coefficient. However, compared to Case 1, the larger total heat transfer area in the B sheet of Case 2 enhances in-tube heat transfer and bubble generation, resulting in a slightly higher boiling heat transfer coefficient in the B sheet.

In Case 3, the boiling heat transfer coefficient in the A sheet increases by 48.24% compared to Case 0, while decreasing by 2.4% in the B sheet. The A sheet features a single flow path through seven 5.2 mm tubes, producing the highest pressure drop among the variable-diameter configurations and the highest average evaporation temperature. While the smaller diameter enhances the boiling heat transfer coefficient, the increased gas-phase fraction at the tube outlet raises flow resistance and reduces velocity. The low refrigerant quality within the small-diameter tubes favors nucleate boiling as the dominant regime. However, at low evaporation temperatures, saturated boiling is suppressed, and the heat transfer enhancement at the tube end is less pronounced than in Cases 1 and 2, where fewer small-diameter tubes are used. Thus, while the A sheet boiling heat transfer coefficient exceeds that of Case 0, it does not reach the levels of Cases 1 and 2. Moreover, the larger gas-phase volume entering the B sheet promotes earlier mist flow, increasing flow resistance and convective heat transfer resistance, leading to a lower boiling heat transfer coefficient than in Case 0.

4.3 Characterization of Pressure Drop in Tubes of Heat Exchangers with Variable Tube Diameters

Pressure drop is a key parameter governing refrigerant flow behavior. Reducing pressure drop lowers the average evaporation temperature and tube wall temperature, thereby improving COP. Relative to Case 0, the total pressure drop in Case 1 increases by 70.47%, concentrated primarily in the 5.2 mm tubes of the A sheet, where the pressure drop is 4.92 times that of Case 0. This results in a 1.28°C rise in the average evaporation temperature and a 0.9°C rise in tube wall temperature. The smaller number of small-diameter tubes in Case 1 limits the pressure drop penalty. The reduced tube diameter increases the R290 flow velocity, elevating frictional pressure drop, while the higher evaporation temperature increases gas-phase density, further contributing to the pressure drop.

In Case 2, the single-flow-path pressure drop increases by 119.95% compared to Case 0. The pressure drops in the A and B sheets are 7.79 and 1.03 times those of Case 0, respectively. The average evaporation temperature in the A sheet rises by 1.3°C, and the tube wall temperature rises by 0.84°C. The increased two-phase flow velocity amplifies frictional losses, while the higher evaporation temperature enlarges the gas-phase fraction, further increasing pressure drop.

Case 3 exhibits the highest pressure drop among all configurations, with a total increase of 129.22% relative to Case 0. The pressure drops in the A and B sheets are 8.87 and 0.92 times those of Case 0, respectively. The larger number of 5.2 mm tubes in the flow path increases frictional resistance. Although the boiling heat transfer coefficient in the A sheet is higher than in Case 0, it is lower than in Cases 1 and 2. The average evaporation temperature and tube wall temperature in the small-tube section rise by 1.29°C and 0.73°C, respectively.

4.4 Optimization Results for Heat Exchangers with Variable Tube Diameters

Based on the comparative analysis of heat transfer, pressure drop, copper savings, refrigerant charge, and COP, the performance of the R290 variable-diameter tube heat exchangers is summarized in Table 9. All variable-diameter configurations exhibit enhanced heat transfer relative to the baseline. Among them, Case 2 achieves the highest overall heat transfer performance and COP, while Case 3 offers the greatest copper savings and lowest refrigerant charge. From an energy efficiency perspective, Case 2 is recommended. Case 3 may be selected to reduce production costs and mitigate usage risks while still realizing energy-saving benefits.

Table 9: Optimization results of variable tube diameter heat exchanger scheme for R290 indoor unit.

	Copper Saving %	Elevated Heat Exchanger Capacity/%	Reduction of the Volume Inside the Tube/%	COP
case0	/	/	/	4.01
case1	7.78	1.91	11.5	4.09
case2	3.62	3.75	7.66	4.16
case3	6.6	3.09	11.32	4.13

5 Conclusions

This study investigates the structural design and performance of a finned-tube heat exchanger for split air conditioning (SAC) indoor units, featuring an innovative configuration that combines tubes of two diameters (5.2 mm and 7.3 mm). This hybrid design aims to enhance heat transfer performance while reducing copper consumption and refrigerant charge. The heat transfer and fluid flow characteristics of this variable-diameter heat exchanger using R290 are analyzed under rated cooling conditions.

(1) A theoretical calculation method is proposed for the variable-diameter heat exchanger. This iterative algorithm determines key parameters-including refrigerant pressure drop, tube wall temperature, and heat exchanger capacity—using the refrigerant outlet temperature as a boundary condition. The converged wall temperature serves as a critical input for subsequent numerical simulations, while the other outputs aid in determining air-side latent heat transfer. The theoretical results demonstrate high reliability.
(2) The accuracy of the theoretical method is verified through a numerical simulation model validated against experimental data from a baseline heat exchanger with 7.3 mm tubes. A grid independence study ensures computational accuracy, and strong agreement between simulation and experimental results confirms the model's reliability.
(3) Accordingly, a combined approach integrating the theoretical correlation-based method with detailed numerical simulation is recommended for performance analysis of such variable-diameter heat exchangers.
(4) Compared with the baseline (Case0), the proposed designs achieve the following performance improvements:Refrigerant (R290) charge reduction: Case 1: 11.5%; Case 2: 7.66%; Case 3: 11.32%; Copper material reduction: Case 1: 7.78%; Case 2: 3.62%; Case 3: 6.6%; System COP improvement: Case 1: 2.0%; Case 2: 3.75%; Case 3: 3.0%.

Among the configurations, Case 2 exhibits superior heat transfer performance and the highest COP, making it recommended for maximizing energy efficiency. Case 3 achieves the greatest copper savings and the lowest refrigerant charge, representing the optimal solution for minimizing material cost and environmental impact.

While this study provides a comprehensive analysis under rated cooling conditions, several limitations remain to be addressed in future research. First, the current investigation is limited to steady-state operation; transient behavior during startup, shutdown, and cycling conditions warrants further exploration. Second, the experimental validation was conducted only on a baseline configuration with uniform tube diameters; direct experimental validation of the proposed variable-diameter designs is necessary to confirm the predictive accuracy of the combined theoretical–numerical approach. Third, the long-term reliability and durability of the hybrid tube configuration under fouling, corrosion, and thermal cycling conditions have not been evaluated. Additionally, the applicability of the proposed design under off-design conditions—such as variable refrigerant flow, part-load operation, and extreme ambient temperatures—should be examined to establish its practical viability across diverse operating scenarios. Addressing these aspects will be critical for advancing the variable-diameter heat exchanger toward commercial implementation.

Acknowledgement: The authors would like to thank the School of Mechanical and Electrical Engineering, Zhoukou Normal University for their support.

Funding Statement: The authors would like to acknowledge the Scientific and Technological Research Projects in Henan Province (No. 262102321095) and the scientific research foundation for high-level talents of Zhoukou Normal University (No. ZKNUC2024018) for grants and supports.

Author Contributions: Conceptualization, Zheming Cheng and Xinping Ouyang; Methodology, Zheming Cheng; Software, Zheming Cheng; Validation, Zheming Cheng, Xinping Ouyang and Zihao Wang; Form analysis, Zheming Cheng; Investigation, Zheming Cheng; Resources, Xinping Ouyang and Ke Sun; Datacuration, Zheming Cheng; Writing-original draft preparation, Zheming Cheng and Zihao Wang; Writing-review and editing, Zheming Cheng and Ke Sun; Visualization, Zheming Cheng; Supervision, Xinping Ouyang and Leren Tao; Funding acquisition, Zheming Cheng and Xinping Ouyang. All authors reviewed and approved the final version of the manuscript.

Availability of Data and Materials: Not applicable.

Ethics Approval: Not applicable.

Conflicts of Interest: The authors declare no conflicts of interest.

Nomenclature

C_p	Specific heat capacity (J/(kg·K))	ΔT_m	Average heat transfer temperature (°C)
d_b	Fin root diameter (mm)	T_w	Tube wall temperature (°C)
d_i	Inner diameter of the tube (mm)	$\vec{u}$	Velocity vector
d_w	Humidity ratio (kg/kg)	$\overline{x}$	Average dryness
F	Volume force (N)	$\dot{x}$	Two-phase fluid mixture dryness
g_i	Unit mass velocity (kg/s)	j_4, j_5, j_6, j_7	Performance coefficient
h_w	Enthalpy (kJ/kg)	v_1	Specific volume of wet air (m^3/kg)
K_0	Heat transfer coefficient (W/(m^2·K))	δ_f	Fin thickness (mm)
l	Tube length (mm)	φ_w	Relative humidity (%)
$\dot{m}_2$	Refrigerant mass flow rate (kg/s)	ρ_L, ρ_G	Liquid and vapor density (kg/m^3)
N	Rows of heat exchanger tube	Pr_L	Liquid Prandtl number
n	Number of flows	β	Ribification coefficient
P	Pressure (kPa)	μ_L, μ_G	Dynamic viscosity (Pa·s)
P_0	Evaporating pressure (kPa)	Re_L	Liquid Reynolds number
Q_0	Assumed heat exchange (W)	σ	Surface tension (mN/m)
q_i	Heat flux (W/m^2)	α_L	Convective heat transfer coefficient (W/(m^2·K))
q_{va}	Air Volume Flow Rate (m^3/h)	λ	Thermal conductivity (W/m·K)
R	External thermal resistance (m^2·K/W)	δ/f	Liquid thickness and fin height ratio
r_0	Latent heat of evaporation (kJ/kg)	$\sigma_{2,3}$	Ratio of cross-sectional area
s_f	Fin pitch (mm)	d_F/d_Z	Pressure drop gradient
s_h	Open slit height (mm)	ϕ_{LO}^2	Two-phase flow factor
s_s	Open slit width (mm)	ε, ε_E, S, We Γ_{Exp}, f_{Exp}	Empirical coefficient
S_T	Viscous dissipation term (W/m^3)	τ	Viscous stress (Pa)
T	Thermodynamic temperature (°C)	κ	Fluid heat transfer coefficient (W/(m^2·K))
t	Time (s)	ρ	Fluid density (kg/m^3)
∇	Hamiltonian operator	s_1	the horizontal tube spacing (mm)
s_1	the vertical tube spacing, mm		

References

1. Ashour AM, Ali Kadhim S, Hilali Jaghdam I, Hammoodi KA, Jaffar HM, Al-Ghezi MKS, et al. AI-assisted performance analysis of mini-split air conditioning units: Experimental and predictive approaches. Int J Refrig. 2026;181:33–46. [CrossRef].
2. Özer Ö, Kumlutaş D. Experimental investigation on cross flow fan's casing parameters inside of a split air conditioner indoor unit by Stereo Particle Image Velocimetry. Appl Therm Eng. 2017;124:1233–46. [CrossRef].
3. Zou T, Zhan D, Hu X, Hu S, Li Y. Experimental and numerical study of cross-flow fan in air-conditioner indoor unit. Int J Refrig. 2022;141:102–11. [CrossRef].
4. Feleke DS, Getie MZ, Minale TA. Numerical investigation of louver edges effect on the performances of louvered fin compact heat exchanger. Heliyon. 2024;10(6):e27254. [CrossRef].
5. Torbarina F, Trp A, Lenić K. Numerical analysis of geometry influence on heat transfer in a slotted fin and tube heat exchanger. Heat Transf Eng. 2023;44(5):411–25. [CrossRef].
6. Batista J, Trp A, Lenic K, Kirincic M. The influence of geometry parameters of rectangular *Vortex* generators on the air-to-water fin-and-tube heat exchanger efficiency enhancement. Int Commun Heat Mass Transf. 2025;162:108647. [CrossRef].

7. Matuszczak M, Nycz K, Mazurek W, Krowicki P, Pietrowicz S, Pandelidis D. Experimental comparison of finned tube heat exchangers for heat rejection under natural convection conditions. Int Commun Heat Mass Transf. 2024;154:107461. [CrossRef].
8. Zhang T, Su M, Zhang H, Liu C, Ouyang X. Design and simulation of a new type of fin-and-tube heat exchanger with trapezoidal slit fins. Case Stud Therm Eng. 2024;59:104604. [CrossRef].
9. Wei W, Xu G, Wang Y, Ding E. Study on air-side performance of air-cooled heat exchangers under large air velocity and wet conditions. Therm Sci Eng Prog. 2024;48:102389. [CrossRef].
10. Azzouz R, Hamida M. Natural convection in a circular enclosure with four cylinders under magnetic field: Application to heat exchanger. Processes. 2023;11(8):2444. [CrossRef].
11. Cho JM, Kim YJ, Kim MS. Experimental studies on the characteristics of evaporative heat transfer and pressure drop of CO_2/propane mixtures in horizontal and vertical smooth and micro-fin tubes. Int J Refrig. 2010;33(1):170–9. [CrossRef].
12. Alnaimat F, Hanan A, Mathew B. Experimental study of flow boiling heat transfer in smooth and circular pin-fin minichannels. Case Stud Therm Eng. 2026;81:107958. [CrossRef].
13. Celen A, Çebi A, Dalkılıç AS. Investigation of boiling heat transfer characteristics of R134a flowing in smooth and microfin tubes. Int Commun Heat Mass Transf. 2018;93:21–33. [CrossRef].
14. Oh JT, Pamitran AS, Choi KI, Hrnjak P. Experimental investigation on two-phase flow boiling heat transfer of five refrigerants in horizontal small tubes of 0.5, 1.5 and 3.0 mm inner diameters. Int J Heat Mass Transf. 2011;54(9–10):2080–8. [CrossRef].
15. Wu JM, Tao WQ. Impact of delta winglet *Vortex* generators on the performance of a novel fin-tube surfaces with two rows of tubes in different diameters. Energy Convers Manag. 2011;52(8–9):2895–901. [CrossRef].
16. Cheng Z, OuYang X, Tao L, Wang Z, Sun K. Optimization design and numerical simulation of variable tube diameter heat exchanger for split air conditioning indoor unit. Front Heat Mass Transf. 2026;24(1):14. [CrossRef].
17. Dhamodharan P, Salman M, Prabakaran R, Kim SC. Comparative analysis of R290 and R1234yf cooling performance in offset strip-fin plate heat exchanger for electric-vehicle battery thermal management. Int Commun Heat Mass Transf. 2024;157:107708. [CrossRef].
18. ANSI/ASHRAE. ANSI/ASHRAE Standart 34-2010 Designation and safety classification of refrigerant. Atlanta, GA, USA: ASHRAE; 2010 [cited 2026 Jan 1]. Available from: https://www.ashrae.org/File%20Library/Technical%20Resources/Standards%20and%20Guidelines/Standards%20Addenda/34_2010_Final.pdf.
19. Kays WM, London AL. Compact heat exchangers. 3rd ed. New York, NY, USA: McGraw-Hill Book Company; 1984.
20. Tang W, Li W. A new heat transfer model for flow boiling of refrigerants in micro-fin tubes. Int J Heat Mass Transf. 2018;126:1067–78. [CrossRef].
21. ASHRAE handbook—Fundamentals. Atlanta, GA, USA: ASHRAE; 2017.
22. Ouyang XP, Sun K. Falling film evaporation experiment and data processing method of R1234ze (E) on horizontal enhanced tubes. Int J Refrig. 2022;134:45–54. [CrossRef].
23. Malapure VP, Mitra SK, Bhattacharya A. Numerical investigation of fluid flow and heat transfer over louvered fins in compact heat exchanger. Int J Therm Sci. 2007;46(2):199–211. [CrossRef].
24. Chisholm D. A theoretical basis for the Lockhart-Martinelli correlation for two-phase flow. Int J Heat Mass Transf. 1967;10(12):1767–78. [CrossRef].
25. Schmidt J, Friedel L. Two-phase flow pressure change across sudden expansions in duct areas. Chem Eng Commun. 1996;141–142(1):175–90.[CrossRef].
26. Moffat RJ. Describing the uncertainties in experimental results. Exp Therm Fluid Sci. 1988;1(1):3–17. [CrossRef].